Journal of Geophysical Research: Atmospheres

RESEARCH ARTICLE
10.1029/2018JD028557

Impacts of Snow Darkening by Deposition of Light-Absorbing Aerosols on Hydroclimate of Eurasia During Boreal Spring and Summer

William K. M. Lau[1], Jeong Sang[2], M. K. Kim[2], K. M. Kim[3], R. D. Koster[4], and T. J. Yasunari[5,6]

[1]Earth System Science Interdisciplinary Center, University of Maryland, College Park, MD, USA, [2]Department of Atmospheric Science, Kongju National University, Gongju, South Korea, [3]Laboratory for Atmospheres, NASA Goddard Space Flight Center, Greenbelt, MD, USA, [4]Global Modeling and Assimilation Office, NASA Goddard Space Flight Center, Greenbelt, MD, USA, [5]Faculty of Engineering, Hokkaido University, Sapporo, Japan, [6]Arctic Research Center, Hokkaido University, Sapporo, Japan

Key Points:
- Snow darkening by light-absorbing aerosols spurs accelerated snowmelt, runoff, and warming of Eurasian land during boreal spring
- Land drying persists through summer due to depleted supply of freshwater supply from accelerated snowmelt and increased evaporation
- Atmosphere-land interaction exacerbates the hot and dry climate, enhancing the intensity and frequency of summertime extreme heating days

Supporting Information:
- Supporting Information S1

Correspondence to:
W. K. M. Lau,
wkmlau@umd.edu

Citation:
Lau, W. K. M., Sang, J., Kim, M. K., Kim, K. M., Koster, R. D., & Yasunari, T. J. (2018). Impacts of snow darkening by deposition of light-absorbing aerosols on hydroclimate of Eurasia during boreal spring and summer. *Journal of Geophysical Research: Atmospheres, 123*, 8441–8461. https://doi.org/10.1029/2018JD028557

Received 22 FEB 2018
Accepted 16 JUL 2018
Accepted article online 28 JUL 2018
Published online 18 AUG 2018

Abstract In this study, we used the NASA GEOS-5 climate model to investigate the impact of snow darkening by deposition of light-absorbing aerosols on the hydroclimate of Eurasia during boreal spring and summer. Two sets of 10-member ensemble model integrations with prescribed sea surface temperature were carried out for 10 simulated years (2002–2011); one includes snow-darkening effects (SDE) by light-absorbing aerosols and one does not (NSDE). Differences between the two experiments in the hydroclimates over Eurasia were evaluated. Results show that SDE warming is most pronounced during the melting season due to strong snow-albedo feedback in the vicinity of the retreating seasonal snowline. SDE spurs a wet-first-dry-later modulation of the surface energy and water balances, characterized by an accelerated (days-to-weeks) snowmelt, accompanied by excessive runoff and a warming and wetting of the land (relative to NSDE) during the early melting season. The snowmelt is followed by a fast desiccation of the land during the late melting, and early warming season, and then a prolonged warmer and drier land, through the boreal summer. The prolonged warming is sustained by atmospheric conditions favorable for the development of atmospheric blocking, that is, higher middle-to-upper-tropospheric geopotential height, lower relative humidity, reduced cloudiness, and enhanced atmospheric subsidence. Overall, SDE by light-absorbing aerosols leads to a warmer and drier boreal summer hydroclimate, increasing the frequency of the top 5 and 1% extreme hot days (as defined by NSDE statistics) over western and northern Eurasia by approximately threefold and tenfold, respectively.

1. Introduction

In a warmer climate, the frequency of extreme hot weather, commonly known as heat waves, is expected to increase along with more severe droughts and wildfires, inflicting grave harm to human health and heavy tolls on the environment and society (Beniston & Coauthors, 2007; Girardin et al., 2009; IPCC, 2013; Lau & Nath, 2014; Luber & McGeehin, 2008; Meehl & Tebaldi, 2004; Seneviratne et al., 2006; Trenberth & Fasullo, 2012). In the extratropics, heat waves often occur under strong atmospheric blocking conditions that are characterized by prolonged periods (several days to weeks) of unusually high pressure and temperature coupled with increased atmospheric stability and widespread subsidence (Barriopedro et al., 2011; Black et al., 2004; Lau & Kim, 2012; Tomczyk & Bednorz, 2016). Abnormally dry soil conditions due to deficit in precipitation in the boreal spring can persist into summer through land-atmosphere coupling, leading to higher land surface temperatures and warmer and drier atmosphere in both seasons, enhancing the intensity and duration of heat waves (Ferranti & Viterbo, 2006; Fischer et al., 2007; Koster et al., 2006; Koster et al., 2016; Lau & Kim, 2012; Lorenz et al., 2010; Xue et al., 2012). Snow cover changes over Eurasia have long been known to play an important role in regional and global climate variability, affecting warm season (spring and summer) temperature over Eurasia, as well as summer rainfall over the Asian monsoon region (Barnett et al., 1989; Dutra et al., 2011; Groisman et al., 1994; Hahn & Shukla, 1976; Matsumura & Yamazaki, 2012; Meehl, 1994; Yasunari et al., 1991; Yeh et al., 1983). However, the mechanisms by which snow cover regulates land temperature and soil moisture, affects land surface energy and water budgets, and possibly even imprints itself on the character of Eurasian summertime heat waves are not fully understood (Schubert et al., 2014).

Recently, an increasing body of studies has shown that enhanced solar radiation absorption due to the deposition of light-absorbing aerosols (LAA), for example, mineral dust, black carbon (BC), and organic carbon (OC), onto the snow surface can cause accelerated snowmelt and warming during the spring season in extratropical land (Aoki et al., 2011; Flanner et al., 2007, 2009; Lin et al., 2014; Ménégoz & Coauthors, 2014; Painter et al., 2010; Warren & Wiscombe, 1980; Yasunari et al., 2011; Yasunari & Coauthors, 2013, 2014; Yasunari et al., 2015). LAA-induced accelerated snowmelt may lead to warmer surface temperatures over Eurasia and to increased rainfall in the following summer over the Asian monsoon regions (Lee et al., 2013; Matsumura & Yamazaki, 2012; Yasunari et al., 2015). Up to now, most studies of snow-darkening effect (SDE) have focused on the roles of anthropogenic LAAs in accelerating the melting of glaciers and snowpack in the Arctic and over high mountain regions such as the Tibetan Plateau, the Himalayas, and the Rocky Mountains (Flanner et al., 2009; Jiang et al., 2017; Painter et al., 2010; Qian et al., 2011, 2014). Recently, Yasunari et al. (2011, 2014) implemented the Goddard Snow Impurity Module (GOSWIM) in the GEOS5 GCM, and demonstrated the importance of deposition of ambient (natural + anthropogenic) LAAs such as dust, black carbon, and organic carbon in affecting model snow albedo and climate. Yasunari et al. (2015) examined SDE impacts on Northern Hemisphere continental regions and found substantial warming and drying of land in extratropical Europe, northern East Asia, the Himalayas, and North America. However, the mechanisms of SDE-induced warming and drying and possible impacts on extreme hot weather during the boreal summer were not explored.

In the present study, we examine continental-scale SDE impacts from climate model experiments, focusing specifically on the mechanisms of hydroclimate feedback over Eurasian, during the boreal spring and summer (March–August). Our overall approach is described in section 2. This is followed by an analysis of the seasonal responses of key hydroclimatic variables to SDE radiative forcing (section 3.1), a quantification of changes in regional surface energy and water balances over selected large-scale spatial domains (section 3.2), a consideration of associated changes in atmospheric conditions conducive to heat wave development (section 3.3), and a comparison of model climatology to observations (section 3.4). Conclusions and caveats of our results are presented in section 4.

2. Model and Methods

Given the lack of SDE observations, most studies relating SDE to climate have relied on model simulations. These studies have provided useful working hypotheses regarding SDE impacts on climate, and they have yielded important guidance both on the use of the limited observations available and on the space-time scales and regions where new in situ observations are needed for validation of model results (Dang et al., 2017; Gautam et al., 2013; Qian et al., 2014; Yasunari & Coauthors, 2010). In the same vein, the present study is based on model simulations. Here we use the NASA Goddard Earth Observing System Model Version 5 (GEOS-5) climate model (Rienecker & Coauthors, 2008). The land surface model in GEOS-5 is the Catchment model (Ducharne et al., 2000; Koster et al., 2000), which uses the snowpack model of Lynch-Stieglitz (1994). For the present study, we use the GOSWIM snow darkening physics package which includes radiative transfer calculations of snow albedo and tracks through the snow the mass distributions of deposited constituent aerosols of dust, BC, and OC (Yasunari et al., 2011; Yasunari & Coauthors, 2014). Aerosol emission, transport, and radiative processes are provided by the Goddard Chemistry Aerosol Radiation and Transport (GOCART) module (Chin et al., 2000). The LAAs in GOCART consist of wind-generated mineral desert dust (Ginoux et al., 2001), BC, and OC from anthropogenic and natural sources including fossil fuel and biomass burning (Chin et al., 2000, 2002; Colarco et al., 2010). The modeling of aerosol deposition on snow involves wind transport from the source regions, dry gravitational sedimentation, and large-scale and convective wet scavenging. The version of GEOS-5 used in this study does not include effects of aerosol-cloud interactions (Randles et al., 2013).

Two 10-member ensemble experiments, each member covering 10 simulated years, were carried out with the GEOS5 model at 2° × 2.5° latitude-longitude horizontal resolution and with 72 vertical layers (Yasunari et al., 2015, hereafter referred to as YKLK). All simulations were forced by prescribed observed sea surface temperature from 2002 to 2011 (Reynolds et al., 2002), and each included fully interactive land surface processes. The first experiment (SDE) includes the full utilization of the GOSWIM SDE physics module. The second experiment (referred to as NSDE) is identical to the first except for the absence of SDE physics, that is,

constituents are not tracked in the snowpack, and do not affect the snow's surface albedo. Effects of SDE on hydroclimate are estimated based on anomaly fields, defined as the difference in the ensemble mean climatology of the two experiments (SDE–NSDE), each climatology being based on a full 100 years of simulation (10 years × 10 ensemble members). Atmospheric heating by LAAs are included in both SDE and NSDE. Statistical significance of the results is evaluated using the Welch's *t* test. To quantify solar absorption by different aerosol species in snow, we define a snow impurity absorption coefficient (SIAC) as the product of the mass of aerosols and the mass absorption coefficients (MACs) in snow. The MAC values used here are based on Table S1 of Yasunari and Coauthors (2014). The total SDE strength is expressed as the sum of the SIAC values for dust, BC, and OC.

3. Results

To set the stage for the discussion of the main results, we first briefly review important features of SDE effects on the annual mean Eurasian climate, as reported by YKLK based on the model simulations. The strongest SDE impact as measured by SIAC is found over central Eurasia, with the strongest contribution by mineral dusts from deserts of North Africa and West Asia (Figure S1a), whereas BC has a stronger relative contribution over Western Europe and East Asia, near highly industrial megacities (Figure S1b). By comparison, OC contributes the least SIAC for all regions, generally below 20%, and with the largest values over eastern Siberia and northeastern China.

Figure 1 shows the anomalies in annual mean skin temperature, soil wetness, snow mass, and net shortwave radiation caused by SDE. Warmer surface skin temperature is found over the entire extratropical Eurasia continent, with the most pronounced signal (>2 °C) over western Eurasia, East Asia, and the Tibetan Plateau (Figure 1a). The warming over central China south of 40°N appears excessive and is most likely due to bias in the climatological (control) snow and cloud cover in GEOS5 in these regions (see YKLK for details). Soil wetness anomalies (Figure 1b) show large regional variations, with strong drying over Europe and most of western and northern Eurasia, but with increasing soil wetness over India, China, and southern Russia. Regions with the most pronounced increase in surface skin temperature coincide with those having large reductions in soil wetness and snow mass (Figure 1c). The anomalous surface warming pattern matches well with regions showing large increases in surface solar radiation over Eurasia, East Asian, and the Tibet-Himalayas region, where the maximum increase of shortwave radiation due to SDE exceeds 10 Wm^{-2} in the annual mean (Figure 1d).

3.1. Seasonal Variations in Hydroclimate

Figure 2 shows latitude-time cross sections (20–80°N), averaged over 10–140°E longitudes, of the SDE-induced anomalous daily surface skin temperature T_s, along with associated changes in net surface shortwave radiation, soil wetness (top 2 cm), and snowmelt rate. The annual mean changes of T_s and soil wetness are shown separately in the right panels for reference. In the annual mean (Figure 2a, right panel), extensive SDE-induced surface warming can be found over the Eurasia continent north of 25°N, with an average of +0.7 °C over the entire continent and with a maximum of +1.4 °C near 50°N. The maximum anomalous seasonal warming, starting near 40°N around mid-March, advances northward reaching near 75°N by the end of August. The warming tracks closely the movement of the shortwave (SW) maximum (contour in Figure 2a). Within the 40–60°N latitude band, the maximum warming and SW absorption advances poleward from April to early June. At higher latitudes (65–75°N), the anomalous warming and surface shortwave absorption starts in mid-June, reaches a maximum in early July, and ends near mid-August. It is interesting to note that near 35°N, the warming and increased SW absorption starts in mid-May and lasts through the summer season into early fall. This latitude belt includes the region of permanent snow cover over the high elevation of the western Himalayas (see Figure 1). Because GOSWIM used here does not include SDE over permanent ice, the effect here is limited to regions with seasonal snowpack over the TP. Extra caution must thus be exercised in interpreting results for this region.

Coupled to the surface warming, the SDE induces annual mean drying of the land (Figure 2b, right panel) in two latitude belts, one in midlatitudes (40–60°N), and one in polar region (60–80°N), whereas it wets the land south of 40°N. The soil wetting in the subtropics and tropics is related to an increase in large-scale moisture transport and precipitation in these regions (see YKLK for details). The soil wetness and snowmelt seasonal change patterns tracking closely those of the temperature and surface shortwave radiation, for example,

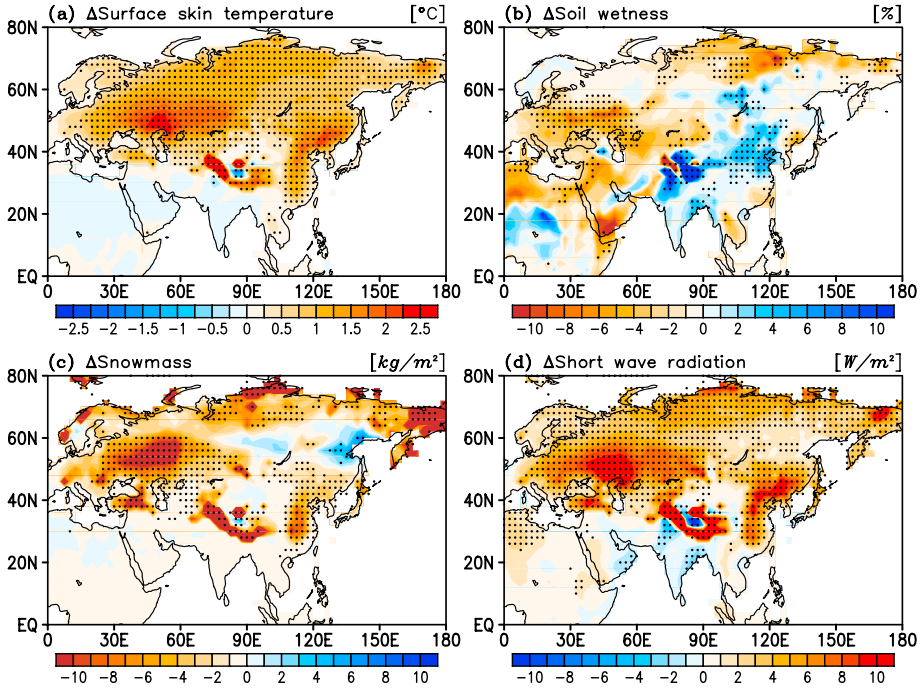

Figure 1. Annual mean change induced by SDE in (a) surface skin temperature (°C), (b) wetness of top (2 cm) soil layer (%), (c) snow mass (kg m^{-2}), and (d) surface shortwave radiation (Wm^{-2}). Dots represent significance at 95% confidence level.

increased snowmelt and soil wetting followed by reduced snowmelt and drying (Figure 2b). It is possible that the initial anomalous soil wetting is due to the accelerated snowmelt and the associated increase in soil water percolation as a result of the warming and thawing of the frozen soil. Snow-albedo feedback, by the way, is

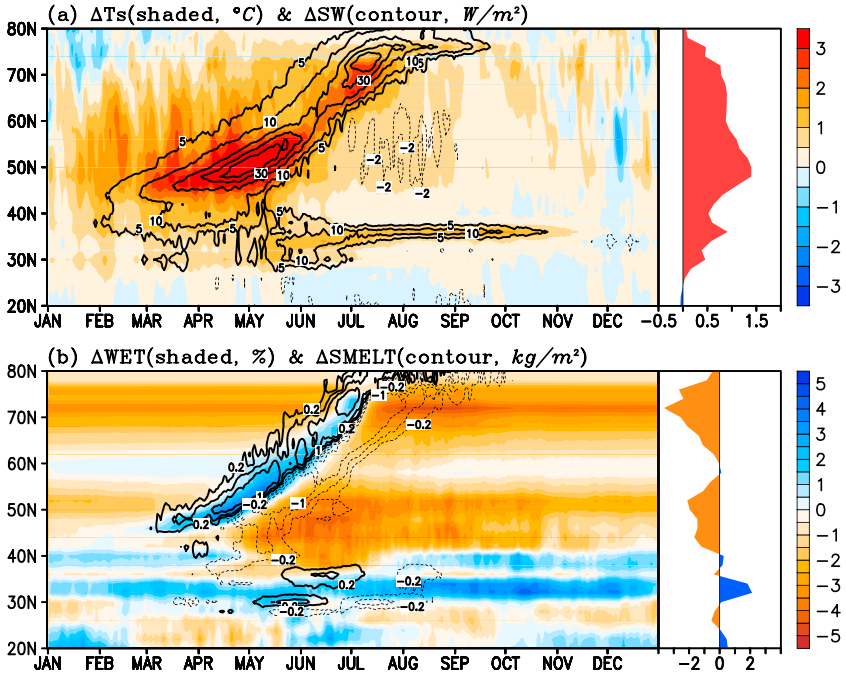

Figure 2. Latitude-time cross sections of anomalies in seasonal variations of zonal mean (10–140°E) daily values of (a) surface skin temperature (°C; shaded) and surface shortwave radiation (Wm^{-2}; contour) and (b) soil wetness (%; shaded) and snowmelt (mm day^{-1}; contour). The annual mean changes are shown on the right panels for (top) surface skin temperature and (bottom) soil wetness, respectively.

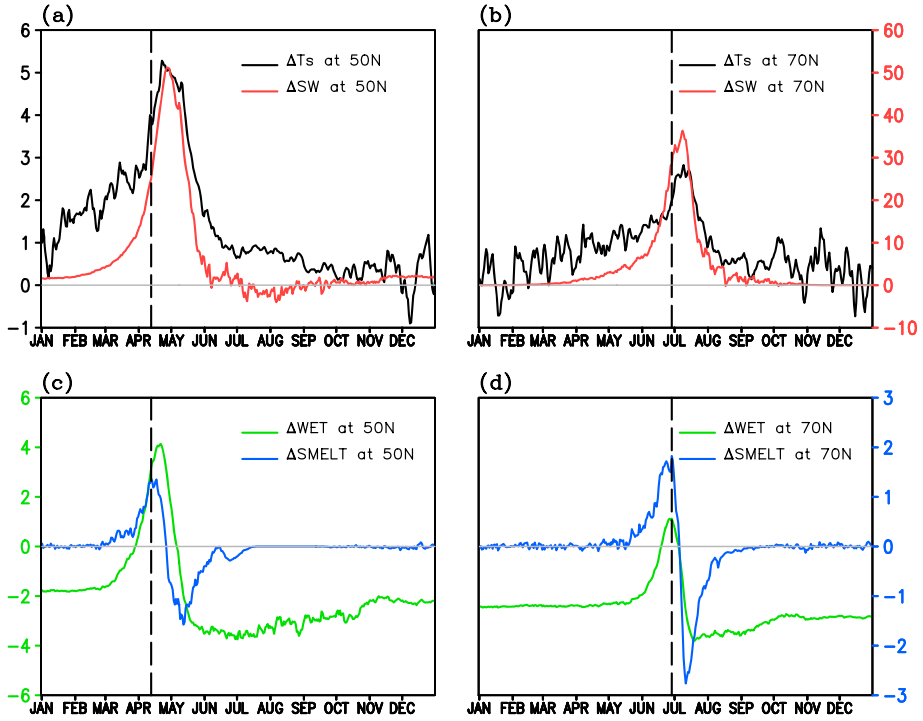

Figure 3. Time series of (a) anomalous skin temperature (°C; black) and net surface shortwave radiation (Wm^{-2}; red) at 50°N. (b) Same as in (a), except for at 70°N. (c) Anomalous snowmelt (mm day^{-1}; blue) and soil wetness (%; green) at 50°N. (d) Same as in (c) except of at 70°N. Thick vertical dashed line marks the timing of the maximum anomalous snowmelt.

likely to play an important role in accelerating the snowmelt even beyond the rates induced directly by SDE. As more areas of dark bare soil are exposed through snowmelt, the overall albedo decreases even more, intensifying the surface warming and further accelerating snowmelt.

Starting from the melting season, the anomalous wetting and drying of the soil (relative to NSDE) appear to follow closely a wet-first-dry-later (WFDL) equilibration process, as the zone of maximum melting migrates poleward following the movement of the snowline over Eurasia from March to August. As a result, WFDL is a strong function of latitude and phase of the seasonal cycle. To wit, over midlatitude Eurasia (50°N; Figure 3a), net surface SW radiation ramps up quickly beginning early March, reaching a maximum in late April to early May, and dropping off quickly thereafter through July. The land warming follows the SW forcing, but show a slower rise and fall, because of equilibration of the water and energy seasonal cycles of land-atmosphere system, and feedback effects to be discussed in the following sections. Maximum anomalous snowmelt and land wetting (Figure 3c) occur in middle-to-late April, slightly ahead of the maximum warming. In fact, at the time of maximum heating, the land is already beginning to dry down, due to loss snowmelt water (Figure 3c) and increased evaporation (see later discussion). The land drying persists through the summer, extending to the following cold season. The top soil remains drier through the winter season because little or no snow melting occur in the winter, and the land is insolated from the atmosphere by the snow cover. SDE surface SW forcing during winter is small, because new clean snow cover is formed, after each new snowfall. We find no significant change in wintertime snowfall in our experiments. This is likely due to our idealized experimental design, which is focused on teasing out the SDE effect on the atmosphere-land interactions, while feedback from other change agents, for example, seas surface temperature, sea ice, and anthropogenic emissions, are not allowed. In the real world, when all change agents are in play, changes in snowfall and hence snow mass during winter may also affect soil moisture in spring and summer (Maurer & Bowling, 2014). During winter through spring, some exchange between top frozen soil and deeper soil may also affect the drying process.

At higher latitudes (70°N; Figures 3b and 3d), similar variations in the phases of surface SW forcing, snowmelt, land warming, brief wetting, and the delayed and persistent drying can be seen, except that activity peaks are found in June to early July, due to the late arrival of the snowline at higher latitudes. Another difference is that

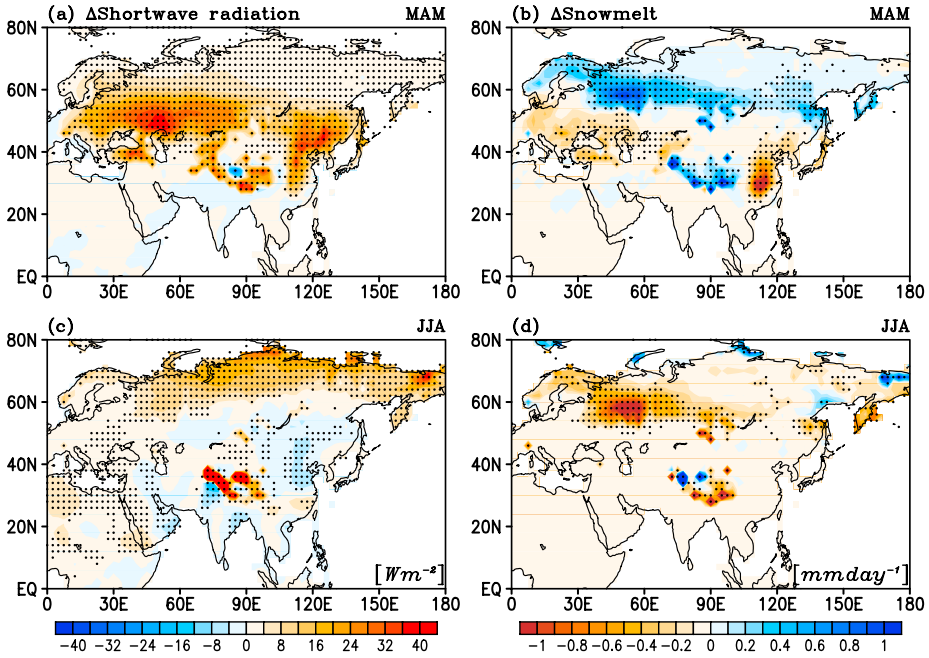

Figure 4. Spatial distributions of SDE-induced anomalies in (a) surface shortwave radiation (Wm^{-2}) and (b) snowmelt ($mm\ day^{-1}$) during MAM. (c and d) The same as (a) and (b), respectively, except for JJA. Dots represent statistical significance at 95% confidence level.

the magnitudes of the SDE induced SW forcing and responses are smaller due to the lesser aerosol loading, and more abundant snow amount at these latitudes. Worth noting here is that a key feature of the WFDL mechanism is the strong asymmetry in the soil wetting and drying processes, with relative fast and short period of enhanced wetting due to snow melting (days to weeks), compared to the slower and prolonged period of drying (again, relative to NSDE) lasting through the summer season and beyond. The rest of the paper is devoted to better understanding of SDE-induced WFDL mechanism in affecting the regional hydroclimates of Eurasia, and the interplay of various land and atmospheric processes in maintaining a new surface water and energy balance under SDE.

First, we examine the impacts of WFDL on changes in seasonal mean climate of Eurasia. During March-April-May (MAM), the strongest SW forcing is found over the latitude band of 40–55°N, as well as in the Tibetan Plateau-Himalayas region (Figure 4a), while the maximum snowmelt has already migrated further north near 55–65°N, as indicated by the north-south dipole-like zonally oriented snowmelt anomalies (Figure 4b). The large SW forcing during MAM at 40–55°N indicates strong snow-albedo feedback due to more exposed bare soil. An exception to the northward migration of the maximum snowmelt zone is found over the Tibetan Plateau-Himalayas region due to its high elevation and prolonged snow season; the region also includes permanent snowpack (Xu et al., 2009). During June-July-August (JJA), the zone of maximum anomalous SW forcing has migrated to the subpolar regions (65–75°N). The negative (relative to NSDE) snowmelt zone was found at 55–65°N, indicating a delayed drying tendency, for example, DL component of WFDL, Here the WFDL effects on snowmelt in the subpolar regions are masked by the three-month JJA average, given the much shorter melting and warming season. The two-month means for May–June (MJ) and June–August (JA), respectively, show clearly the northward migration of the zones of maximum SW forcing and snowmelt from 55 to 60°N in MJ to the subpolar regions in JA (Figure S2).

Figure 5 shows the distribution of surface temperature and soil-wetness anomalies relative to NSDE over Eurasia for MAM and JJA. From MAM, the entire Eurasian continent is warmer (Figure 5a), with a pattern very similar to the surface SW anomalies (see Figure 4a). Increased soil wetness is found in two main regions: (a) the midlatitude belt (50–65°N) spanning northern Europe, Eurasia, and northeastern Asia and (b) the Asian monsoon region, covering the Indian subcontinent and Arabian Peninsular to northeastern China (Figure 5b). The increased soil wetness near 50–65°N is mostly due to increased snowmelt, as is evident

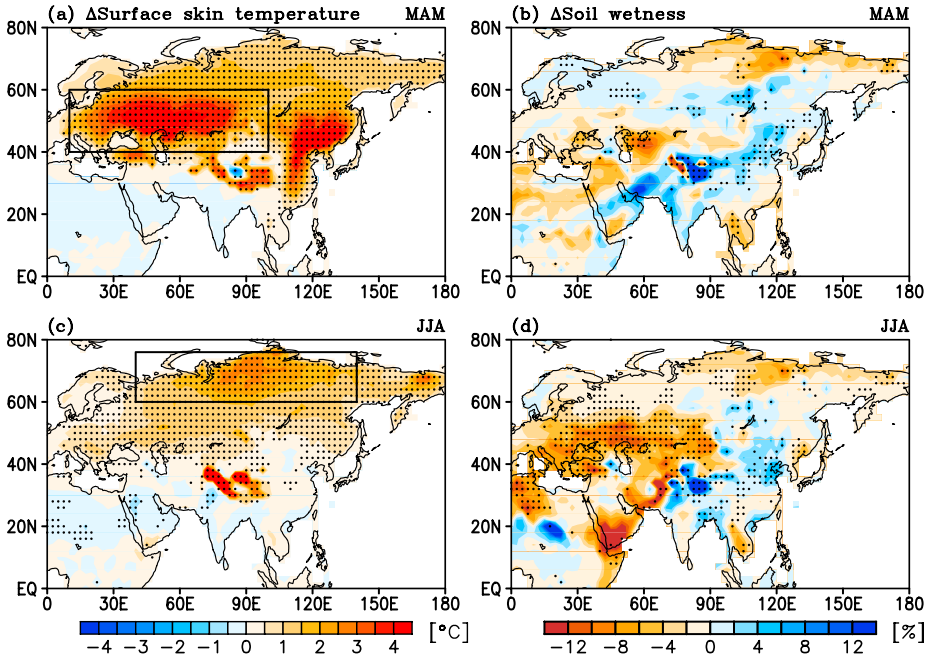

Figure 5. Spatial distributions of SDE-induced anomalies in (a) surface skin temperature (°C) and (b) wetness of top (2 cm) soil layer (%) during MAM. (c and d) The same as (a) and (b), respectively, except for JJA. Dots represent statistical significance at 95% confidence level. Rectangular box in (a) and (b) shows, respectively, the western Eurasia (WE) and northern Europe (NE) domain used for the regional surface energy and water balance analysis.

from its approximate colocation with the maximum snowmelt anomaly (see Figure 4b). Notice that in MAM, land drying (relative to NSDE) has already begun in southern Europe, West Asia, the Middle East, and North Africa. These more southerly regions are either snow free or become snow free much earlier having their relatively scant snow cover rapidly depleted by the accelerated snowmelt. The wetting and drying over the more southern snow-free regions most likely reflect atmospheric teleconnections and hydrologic feedback (Lau & Bua, 1998; Lau & Kim, 2012). During JJA (Figure 5c), the regions of strongest warming lie within polar Eurasian land (60–75°N, 75–120°E) and the southern Tibetan Plateau/Himalayas region, both of which are characterized by a climatologically late melting season. The anomaly pattern of soil wetness (Figure 5d) is complex, with the DL (dry-later) effect dominating over large parts of Eurasia, and with the drying intensified and expanded over regions already drying during MAM, for example, southern Europe, the Middle East, North Africa, and polar Eurasia. An exception is the Asian monsoon region, where soil wetness is increased due to an SDE-induced reduction of snow cover and warmer land in the antecedent boreal spring, which changes the large-scale circulation, transporting a surplus of moisture from the tropical ocean and enhancing the summer monsoon precipitation (Barnett et al., 1989; YKLK).

3.2. Regional Water and Energy Balance

In this section, we examine the SDE-induced changes in domain-averaged daily surface energy and water balances over two regions that showed pronounced warming and drying relative to NSDE (Figure 5), for example, western Eurasia (WE; 10–100°E, 40–60°N) and northern Eurasia (NE; 40–140°E, 60–76°N). As indicated in Figure S1, snow impurities in these two regions consist mainly of dust aerosols (48–55%), with a significant contribution from BC (43–47%). To begin, we illustrate how the WFDL mechanism is manifest in the strong asymmetry in areal-mean wetting versus drying, for example, more drying, less wetting, over large domain that cover a broad latitude band (~15–20 latitudes). As will be shown in the following sections, other factors also contribute to the change in water (and energy) balance over the domain, but enhanced snowmelt from SDE is the primary driver of soil wetness, under our experimental setup. Over WE (Figures 6a and 6c), the southern part of the domain (46°N) gets maximum soil wetting from enhanced snowmelt near mid-March. Regions to the north get maximum wetting progressing later, in mid-April at 50°N, and in mid-May at 56°N. However, the wetting due to increased snowmelt is relatively fast. As the snow cover is being depleted, there is less snowmelt water available for soil wetting, and drying (relative to NSDE) begins. The substantial

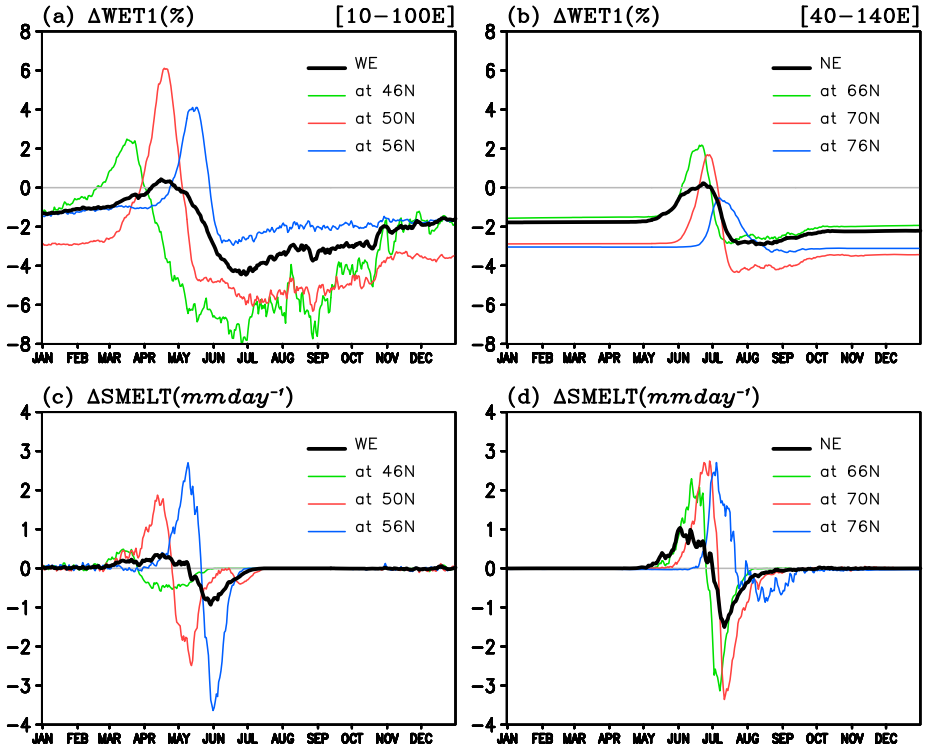

Figure 6. Time series of daily variations of (a) anomalous soil wetness (%) at 46°N, 50°N, and 56°N, respectively, with domain-averaged time series over WE (40–60°N) shown as thick black line. (b) Same as in (a), except at 66°N, 70°N, and 76°N, and domain-averaged over NE (60–76°N). (c and d) The same as (a) and (b), respectively, except for anomalous snowmelt (mm day^{-1}).

reduction in snowmelt water is evident in the large negative swing in snowmelt immediately following maximum snowmelt at all three latitudes, which peaks at progressively later time, in late spring and early summer, as the latitude increases (Figure 6c). Drying from loss of snowmelt water and increased evaporation (see discussion pertaining to Figure 9) already occur in the southern part of the domain, while the northern part is wetting. Drying also tends to maintain through the summer season by land-atmospheric interaction (see later discussion), with a slow, partial recovery through the fall and winter, until the next spring, when the cycle repeats. As a result of the spatial and temporal asymmetry of WFDL, the areal-mean wetting is masked by the more widespread and dominant drying process (thick solid line in Figure 6a). At higher latitudes over NE (Figures 6b and 6d), the asymmetric characteristics of WFDL, for example, the brief but significant wetting at successive later times from low to high latitudes, the ensuing rapid dry-down, followed by the persistent land drying through the summer and beyond, and the masking of the areal-mean wetting, are similar to WE. The main differences are that the anomalies occur later in the season (June–August) and last over a shorter period due to late arrival of the snowline, and the shorter melting season in the subpolar regions.

To better understand the SDE impacts on water and energy balances, we next discuss changes in climatic states of the land and atmosphere that are germane to the maintenance of these balances. Over WE, the domain-averaged land warming is most pronounced (up to ~3°C) during April–May, diminishing rapidly from late May to June, and leveling off to 0.5–1 °C warming during July–August (Figure 7a). Soil moisture exhibits a delayed response, showing a slight wetting during mid-April, but maximum drying during June–August (Figure 7b, reproduced from Figure 6a). As explained in Figure 6, the asymmetry stems from the fact that the maximum land wetting by snowmelt occurs near the retreating snowline on fast time scales, whereas the subsequent drying occurs over expanded areas of reduced or no snow cover over the entire domain. For the entire period, the planetary boundary layer is moistened, as indicated by the increase in the near-surface specific humidity (**q**; Figure 7c) due to enhanced surface evaporation (see later discussion related to Figure 8). However, the boundary layer actually becomes *drier*, as evident in the reduction in relative humidity (RH; Figure 7d). This is due to the fact that saturated water vapor, which is controlled by near-surface

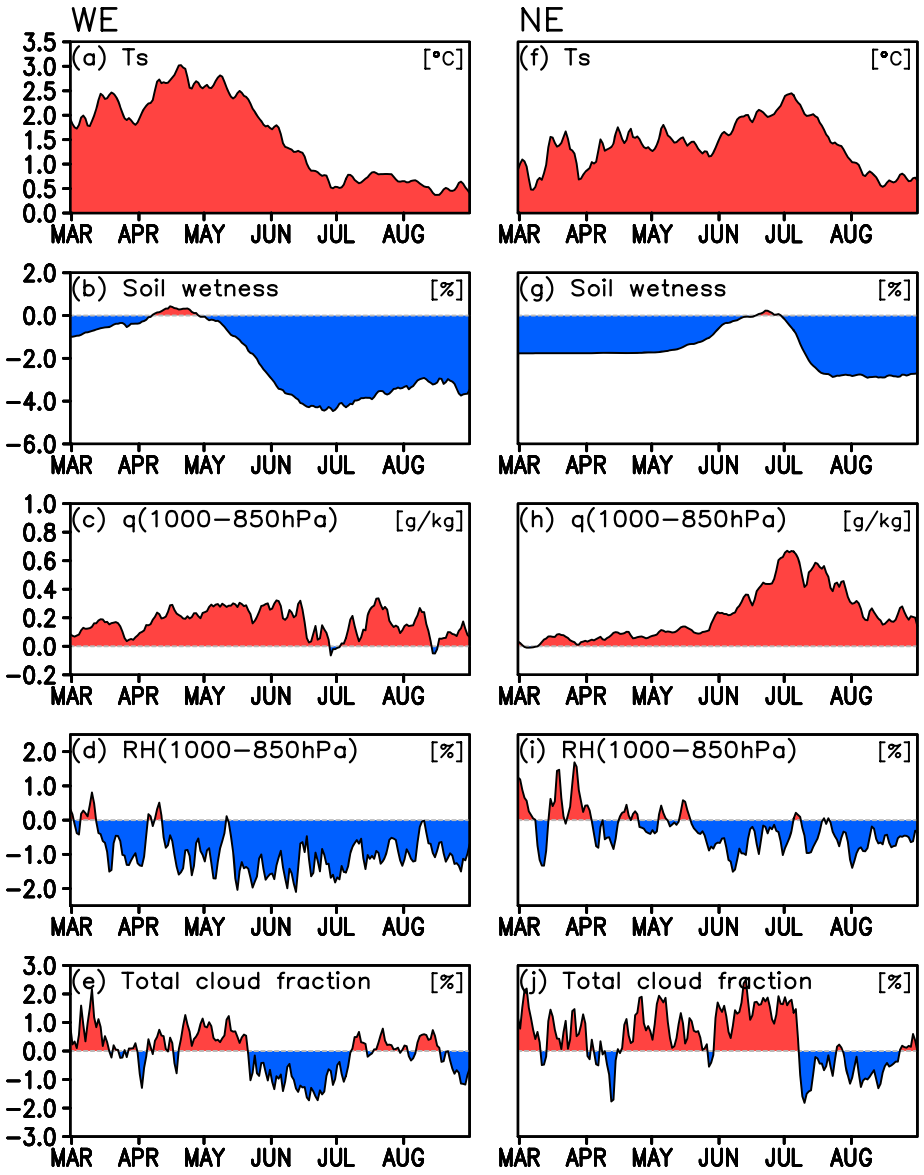

Figure 7. Daily variations of domain-averaged anomalies in (a) surface skin temperature T_s, (b) soil wetness, (c) subcloud layer specific humidity, (d) subcloud layer relative humidity, and (e) total cloud fraction for WE. (f–j) The same as (a)–(e), respectively, except for NE. Positive (negative) values are shaded red (blue).

temperature according to the Clausius-Clapeyron thermodynamic relationship, increases faster than ambient **q**, which depends on increased evaporation and/or moisture transport (Fasullo, 2012; Lau & Kim, 2017). The increase in **q** and in the surface temperature would increase moist static energy in the planetary boundary layer, favoring convection and clouds. The reduction in RH, on the other hand, would require stronger lifting to reach the condensation level, limiting cloud formation. The net result of these two opposing forces is that cloudiness is enhanced during the melting season up to mid-May but is sharply reduced in mid-May through early July with only minor fluctuations thereafter (Figure 7e).

Over NE, the evolving changes of the hydroclimatic states (Figures 7f–7j) are similar to WE, except for the delayed timing of the warming and the more abrupt drying of the land due to the later and shorter melting and warming seasons at higher latitudes. Note, for example, that the maximum land warming (Figure 7f) and increase in **q** (Figure 7h) occur in early July, whereas the maximum soil drying occurs in late June to mid-July, and the land remains dry through August (Figure 7g, reproduced from Figure 6b). Drier atmospheric conditions ($\Delta RH < 0$) prevail from mid-May through end of August (Figure 7i). Cloudiness is increased from March up to early July but is abruptly reduced during the warm season in early July–August (Figure 7j).

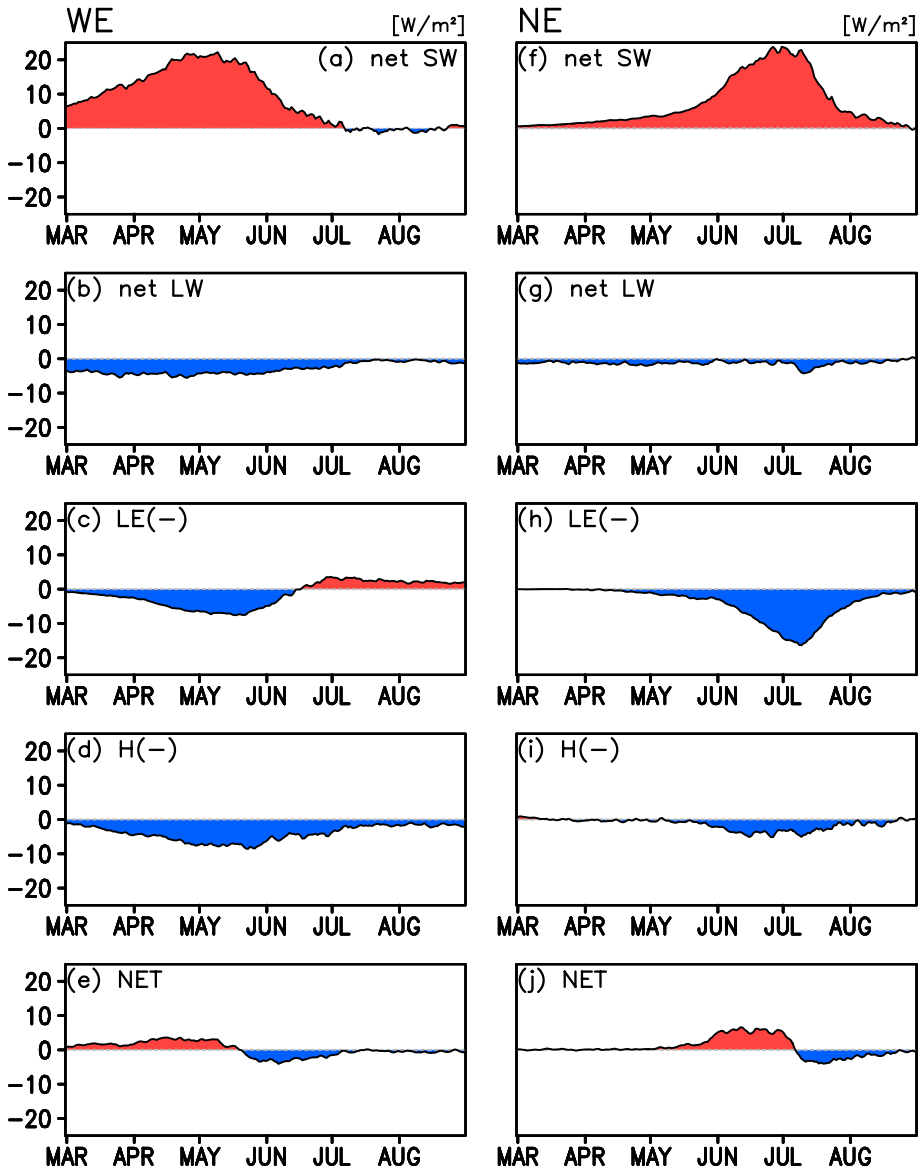

Figure 8. Seasonal variations of daily, domain-averaged changes in components of the surface energy balance (Wm^{-2}) of the top soil layer, for (a) SW, surface shortwave radiation; (b) LW, longwave radiation; (c) *LE*, latent heat flux; (d) *H*, sensible heat flux; and (d) NET, the net energy balance for WE. (f–j) The same as (a)–(e), respectively, except for NE. Positive (negative) flux values represent energy gained (lost) by land and indicated by red (blue) shading.

We now discuss the relationships between the aforementioned hydroclimate changes with the surface energy and water balance of the two regions. The surface energy balance is governed by

$$\mathrm{NET} = \mathrm{SW} + \mathrm{LW} + LE + H, \tag{1}$$

where SW, LW, *LE*, and *H* represent, respectively, the surface shortwave, longwave radiation, latent heat flux, and sensible heat flux, respectively. NET is the net energy flux into the surface layer. All quantities shown are for areal averages computed from 10-year daily means through the seasonal cycle. Over WE, the SDE-induced increase in net surface SW radiation (Figure 8a) is clearly the main driving force of the land warming during the melting season (MAM), reaching a maximum of approximately 20 Wm^{-2} during late April to early May. From late May to June, when much of the surface snow has already melted, the SW warming does not end abruptly, but rather declines slowly. The slow decline is due in part to an increase in net downward SW

Table 1
Change in Heat Balance Components (Wm^{-2}); Surface Skin Temperature, T_s (°C); and Soil Wetness, WET (%) Over Western Eurasia (WE) and Northern Eurasia (NE) in Early Melting Period and Warming Period

		SW	LW	*LE* (−)	*H* (−)	NET	T_s	WET
WE	MAM	14.82	−4.03	−4.33	−4.86	1.60	2.33	−0.57
	JJA	1.77	−1.41	0.87	−2.41	−1.18	0.78	−3.69
NE	MJ	11.22	−1.05	−4.70	−2.12	3.35	1.67	−0.72
	JA	9.63	−1.49	−6.86	−2.45	−1.18*	1.29	−2.42*

Note. SW, LW, *LE*, and *H* represent incoming solar radiation, longwave radiation, latent, and sensible heat flux, respectively. Positive (negative) values indicate gain (loss) by the land surface. The net balance, NET, is computed as the residue of all heat balance components. Asterisk denotes statistical confidence level at 99% (95%).

from reduced cloudiness during this period (see Figure 7e). For the entire period, the surface warming is balanced by cooling due to loss of LW (Figure 8b) and sensible heat flux (*H*; Figure 8d) by the land. Loss of *LE* (Figure 8c) cools the land surface from March to mid-June, but reverses sign; for example, the land gains energy, during July–August, when the SW forcing essentially vanishes (Figure 8a), and the land is warmed due to reduced evaporative cooling from the severely dried land (see Figure 7b). The magnitudes of changes in components of the energy cycle for the melting (MAM) and the warming season (JJA) and corresponding soil moisture changes are tabulated in Table 1. Overall, the WE land surface is characterized by an invigorated surface energy balance, with energy gain by the land from net absorbed SW radiation (+14.82 Wm^{-2}), balanced approximately by energy lost through combined effects of LW (4.03 Wm^{-2}), *LE* (4.33 Wm^{-2}), and *H* (4.86 Wm^{-2}) in conjunction with pronounced strong anomalous surface warming (+2.33 °C) during MAM, and anomalous drying (−3.69%) during JJA.

Over NE, SDE-induced SW warming increases slowly from March to June, ramping up subsequently with maximum warming in late June and early July (Figure 8f). The SW warming tails off slowly in July–August, when reduced cloudiness (see Figure 7j) maintains the warming by allowing more downward SW to reach the surface. During June–July the strong SW warming is balanced in large part by evaporative cooling (Figure 8h). For the entire period, the warming of the land by SW energy gain is in quasi-equilibrium with cooling due to energy loss via LW, LH, and *H* fluxes from land to air (Figures 8g–8j). From Table 1, during the melting season (MJ), the surface warming (+1.67 °C) over NE is pronounced and sustained (+1.29 °C) during the warming season (JA) when the land drying is most pronounced. Overall, the land gains energy (+3.35 Wm^{-2}) during May–June, and losses energy (−1.18 Wm^{-2}) during July–August, resulting in a net gain during spring through summer, as a result of increased land-atmosphere interactions.

The rate of change of soil moisture storage is related to the surface water balance by the following equation:

$$\mathrm{NET} = \mathrm{SM} - R + P - E \tag{2}$$

where SM, *P*, *E*, *R*, and NET represent, respectively, the rates of snowmelt, precipitation, evaporation, runoff, and water flux into the surface layer. All quantities have been computed as areal means over the WE and NE, respectively. Over WE, SDE-induced anomalous snowmelt is the dominant contributor to the rate of change of soil wetness, as evidenced by the similarity in the time evolution of snowmelt (Figure 9a) and the net balance (Figure 9e). Increased snowmelt occurs in March to mid-May, followed by a large reduction from mid-May to June (Figure 9a). The large reduction in snowmelt is due to the accelerated snowmelt earlier in the melting season, which results in reduced snowmelt water (compared to NSDE) available for melting and wetting during May–June. As a result, the land dries rapidly in May–June (see Figure 7b). The net decrease in snowmelt through the entire period (March through June) may also imply a reduction in snowmass before the melting season, associated with the preceding warmer January–February (see Figure 3a). Contemporaneously, the reduced snowmelt leads to decreased runoff, resulting in less soil water lost (relative to NSDE) by runoff, and hence a slight wetting tendency (Figure 9b). However, this effect is small compared to the snowmelt change. Over the entire period, precipitation changes are small, and precipitation and evaporation (Figures 9c and 9d) are approximately balanced, having minimal impacts on the surface water balance. Because of the reduction of freshwater input from snowmelt and the (slight) reduction in precipitation (Figure 9c), the land drying is prolonged through the boreal summer until the next rainy and snowy cold season, exacerbating the climatological warm and dry season (JJA) over WE. The asymmetry of the WFDL effect is evident in NET (Figure 9e), which shows that the WE land surface as a whole slightly gains (strongly loses) water in March–April (May–June). Since NET corresponds to the *rate of change* of soil moisture, this change pattern is consistent in with the moderately positive (strongly negative) *rate of change* in soil wetness (see Figure 7b) during March–April (May–June).

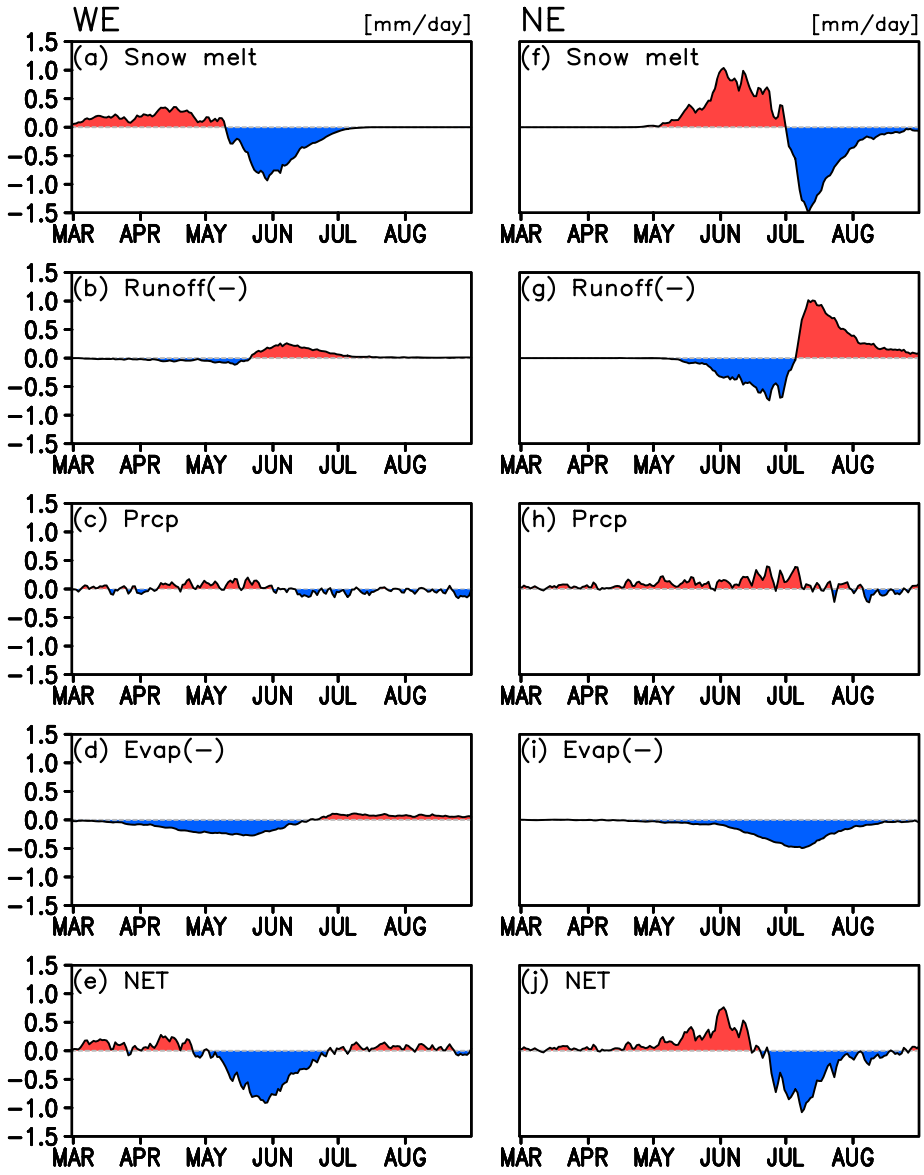

Figure 9. Seasonal variations of daily, domain-averaged changes in surface water balance (mm day^{-1}) for (a) snowmelt, (b) runoff, (c) precipitation, (d) evaporation, and (e) the net water balance of the top (2 cm) layer. (f–j) The same as (a)–(e), respectively, except for NE. Positive (negative) values represent water gained (lost) by land and indicated by red (blue) shading.

Over NE, the dominant impact of SDE-induced snowmelt on the net rate of soil moisture change is again evident in the similarity between Figures 9f and 9j. Here the WFDL forcing by snowmelt is even more pronounced, occurring later in the season (June–August), and over a shorter duration due to its higher-latitude location compared to WE. As in WE, runoff opposes and reduces the magnitude of the WFDL tendency (Figure 9g). A slight increase in precipitation in May–June tends to wet the soil moderately in May–June (Figure 9h). Water loss from enhanced land evaporation maintains and prolongs the land drying in June–July (Figure 9i). Again, the WFDL effect is evident in NET (Figure 9j), which shows that overall, the NE land gains (strongly loses) water from enhanced snowmelt during May to mid-June (mid-June to July), coinciding with positive (negative) *rate of change* of soil wetness (Figure 7g), during the, respectively, periods. While the surface water balance analysis have provided a reasonable account of the regional change in soil wetness induced by SDE snowmelt, it should be noted that transfer of moisture into deeper soil layers may also affect total surface water budget.

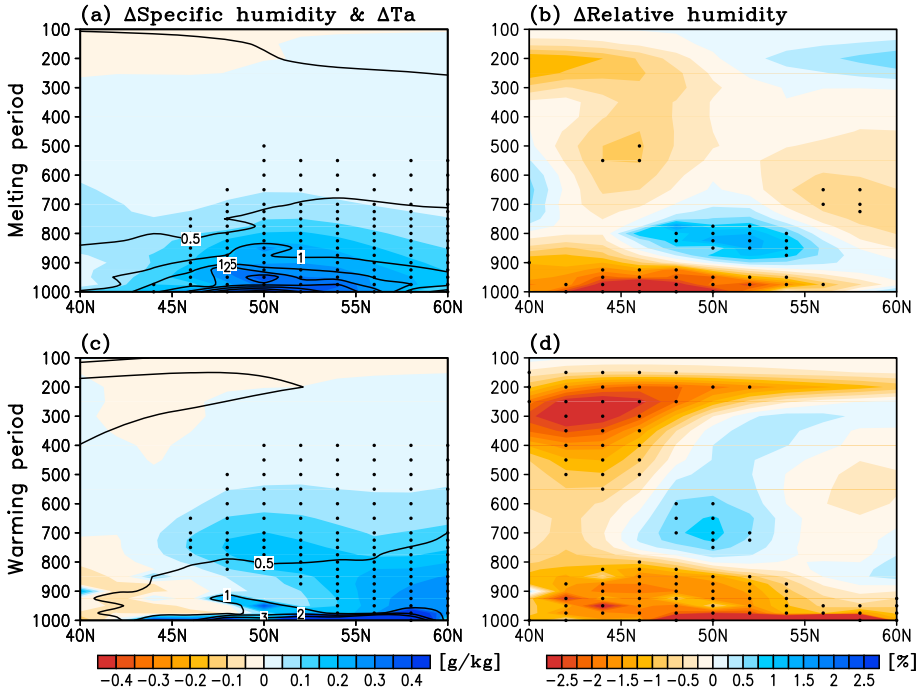

Figure 10. Vertical distribution of changes in (a) specific humidity, **q** (g kg^{-1}; shaded), and air temperature (contour; °C) and (b) relative humidity (%) in MAM for WE. (c and d) The same as (a) and (b), respectively, except in JJA. Black dots indicate statistical significant at 95% confidence level.

3.3. Changes in Atmospheric Conditions

In this section, we examine changes in atmospheric conditions during boreal summer, associated with the SDE-induced WFDL. Here our focus is on changes in the seasonal mean thermodynamic and circulation conditions that are favorable for the development of extreme heating days, but not on the development of specific heat waves and atmospheric blocking events, which are known to involve complex atmospheric feedback including changes in jetstream dynamics, transient-mean flow interactions, and remote forcing from sea surface temperature (Fang & Yang, 2016; Jiang et al., 2017; Nie et al., 2016). The investigation of atmospheric dynamics of heat waves and blocking is outside the scope of this work. Because of the strong latitudinal dependence of the timing and duration of the melting and warming seasons, we identify the melting season as MAM and the warming season as JJA for WE, and as MJ and JA for NE. During the WE melting season (Figure 10a), air temperature and specific humidity are increased near the surface and in the lower troposphere, as a result of increased energy and water input (LW, *LE*, and *H*) from the warmer land. However, because of the rapid warming of the air near the land surface, the rate of increase in saturated specific humidity **q**, which is governed by the Clausius-Clapeyron relationship (~6.5% per degree rise in temperature), is greater than the rate of increase in ambient **q.** As a result, there is a strong reduction in near-surface RH in WE (Figure 10b). During the warming period, **q** in the southern part of WE is reduced but increased in the northern part, reflecting the time delay and latitudinal dependence of the WFDL effect (Figure 10c). The most remarkable feature during the warming season (Figure 10d) is that the near-surface atmospheric drying ($\Delta RH < 0$) that begins in the melting season has become deeper and has expanded over nearly the entire domain, except near the midtroposphere near 45–55°N, where atmospheric moisture is transported by weak westerlies from the Atlantic Ocean during JJA (see YKLK for details). In the southern part of WE, the drying of the atmosphere has extended over the entire troposphere with a maximum in the upper troposphere (400–200 hPa). The drying of the middle and upper troposphere is associated with large-scale subsidence, which is favorable for the development of atmospheric blocking conditions (see discussions pertaining to Figures 12 and 13). These atmospheric temperature and RH anomalies are consistent with the WFDL effect, following the seasonal northward movement of the snowline.

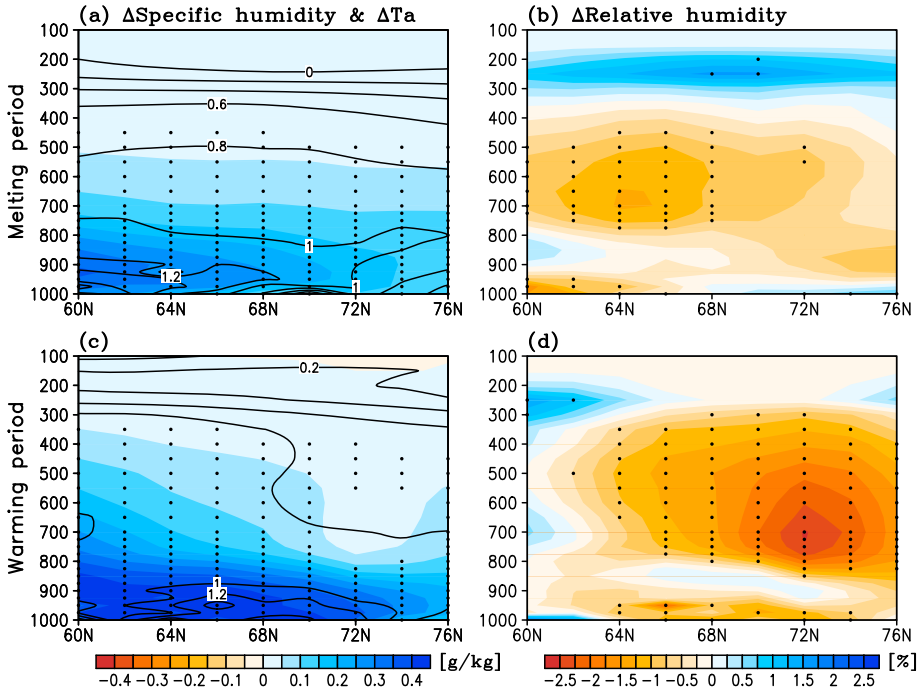

Figure 11. Same as Figure 10 except for NE.

Over NE (Figure 11), overall changes in air temperature, **q**, and RH are similar to those for WE, but with notable differences. During the melting season (MJ), in conjunction with the near-surface warming, SH increases over a deeper layer from the surface (Figure 11a), whereas RH is strongly reduced from 800 to 400 hPa (Figure 11b). During the warming season (JA), **q** continues to increase over the whole domain (Figure 11c), while the

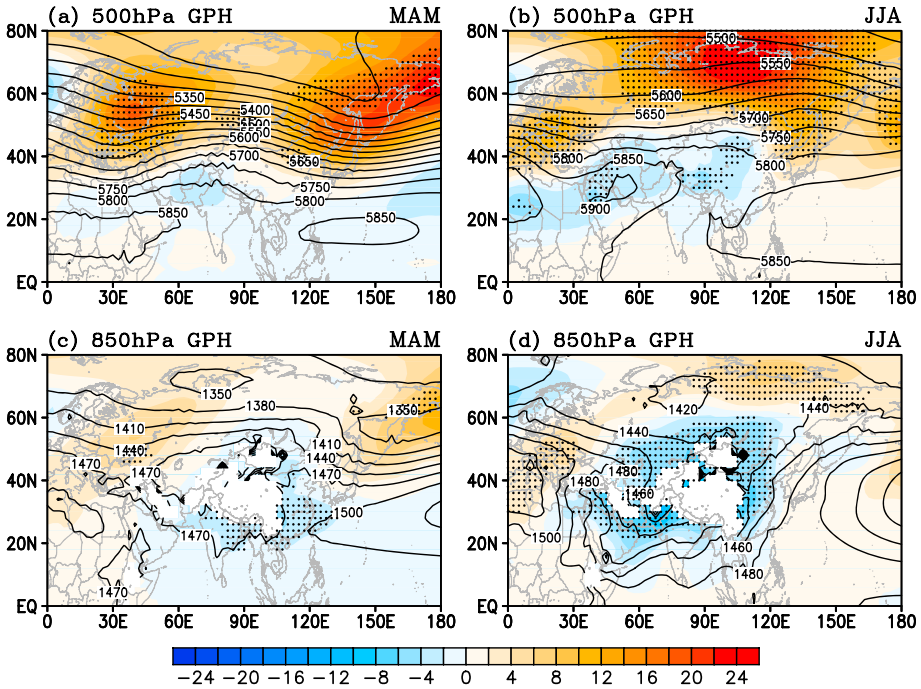

Figure 12. Spatial distribution of SDE geopotential height anomalies (colored) and NSDE climatology (contour) at (a) 500 hPa and (c) 850 hPa in MAM. (b and d) The same as (a) and (c), respectively, except for JJA. Black dots indicate significance at 95% confidence level.

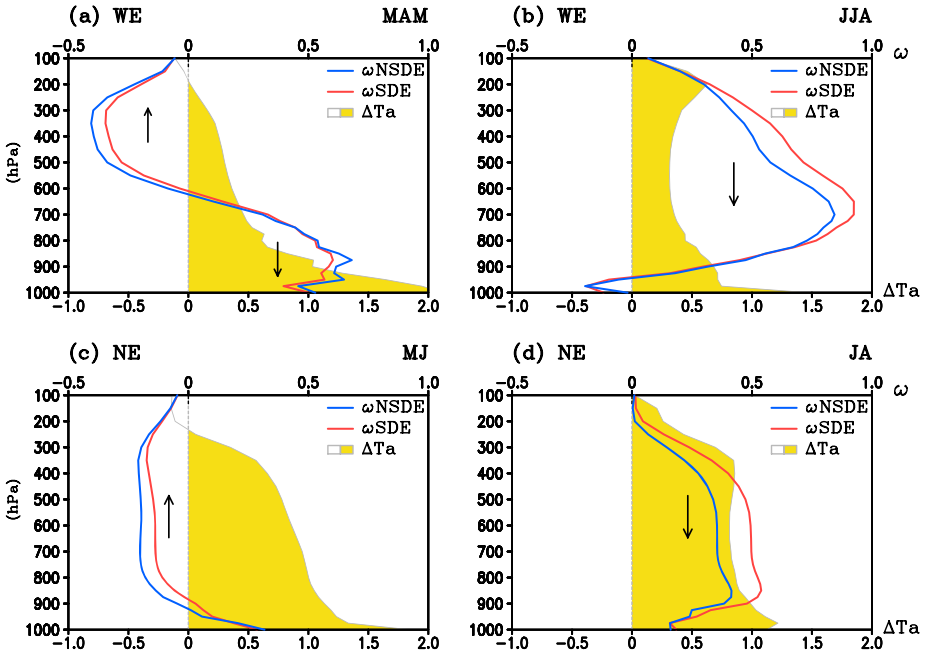

Figure 13. Vertical profiles of climatological *p* velocity (10^{-2} hPa s^{-1}; positive for downward motion) for SDE (red) and NSDE (blue), and atmospheric temperature anomalies (°C) over WE, during (a) MAM and (b) JJA. (c and d) The same as (a) and (b), except over NE during MJ and JA, respectively. Arrow indicates direction of climatological vertical motion.

atmospheric drying (Figure 11d) intensifies and extends over almost the entire troposphere, with a maximum over polar latitudes (70–75°N). The maximum drying is coincident with the time of increased midtropospheric warming and subsidence associated the development of atmospheric high-pressure conditions (see Figure 12). Over both regions, the drier atmosphere suppresses precipitation and clouds, sustaining longer periods of clear-sky conditions and increasing surface net solar radiation absorption and warming of the land.

Next, we use geopotential height and large-scale vertical velocity at 500 hPa to identify changes in large-scale circulation conditions associated with SDE-induced surface warming (Barriopedro et al., 2011; Black et al., 2004; Lau & Kim, 2012). During MAM (Figure 12a), SDE induces coincident high-pressure anomalies in the upper (not shown), middle, and lower troposphere, as evidenced by a barotropic structure with two action centers, one over central Europe and one over the Sea of Okhotsk. The high-pressure situation is generally associated with large-scale subsidence and adiabatic warming of the atmosphere, as well as with reduced tropospheric RH and suppressed clouds (see Figure 7). In conjunction with the two high-pressure centers, a large-scale low-pressure center in the lower troposphere is established over the Asian monsoon region (Figure 12c). During JJA, the high-pressure pattern becomes more intense and organized, with the two high centers shifted to the Siberian region in NE and over the WE domain. At the same time, the low center over the Asian monsoon region intensifies and expands, covering the Asian monsoon and adjacent land regions (Figure 12d). As noted in YKLK, the enhanced large-scale low-pressure pattern is responsible for the SDE-induced increases in moisture transport and summer precipitation in the Asian monsoon region.

The geopotential height anomalies are closely tied to changes in surface and air temperature and large-sale vertical motion. During the melting season (MAM), warming over WE (Figure 13a) is strongest at the surface (~2.0 °C) due to strong SW absorption and decreases rapidly with height up to 200 hPa. The warming in atmosphere is accompanied by anomalous downward motion (reduced climatological upward motion) in the middle-to-upper troposphere, 600–200 hPa. Below 800 hPa, anomalous upward motion (reduced climatological downward motion) is found, consistent with an increase in low-level convective instability, associated with increase in subcloud specific humidity, total cloudiness, and surface evaporation (see Figures 7d, 7e, 8c, and 9d). During JJA (Figure 13b), the near-surface warming (~1.0 °C) is substantially reduced from MAM due to the diminished SDE-induced surface SW absorption, while the climatological strong subsidence in NSDE is further enhanced under SDE. Adiabatic warming by the enhanced subsidence in the atmosphere layer between 800 and 200 hPa will likely sustain the atmospheric warming there. The anomalous

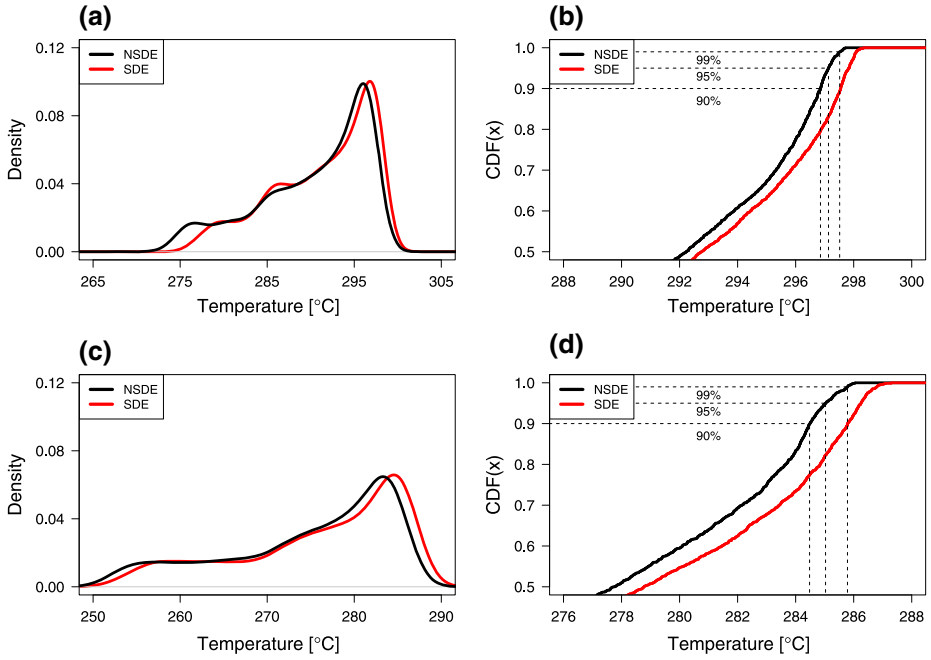

Figure 14. Surface skin temperature distribution shown as (a) probability density function and (b) cumulative distribution function, for WE, under NSDE (black) and SDE (red), respectively. Changes in frequency of 10, 5, and 1% extreme temperature events, as defined by NSDE thresholds, are highlighted. (c and d) The same as (a) and (b), except over NE.

subsidence will also transport drier air from above, and further contribute to the reduction in RH and cloudiness (see Figures 7d and 7e), providing a positive feedback to the WFDL effect during the warm season. Over NE (Figures 13c and 13d), the relationships between surface and atmospheric warming and vertical motions for the melting (MJ) and warming (JA) seasons are very similar to those for WE. Here the warming of the atmosphere by enhanced subsidence in MJ and JA is even stronger, extending throughout the entire troposphere, suggesting increased sensitivity of atmospheric warming to SDE at higher latitudes.

To quantify SDE effects on extreme temperature, we have examined the changes in the probability distribution function (pdf) and cumulative distribution function (cdf) of skin temperature for WE and NE, respectively. For both regions, the pdfs (Figures 14a and 14c) show a clear shift toward warmer temperature, with a stronger signal in NE compared to WE. The cdfs (Figures 14b and 14d) show quantitatively the shift in probability distribution toward higher extreme temperatures. For example, in WE (Figure 14b), the threshold value for a top 10% event under NSDE becomes the threshold value for a top 20% event under SDE, which implies that SDE induces a doubling in the frequency of temperatures exceeding this value. Table 2 summarizes the changes in probability of occurrence of top 10, 5, and 1% extreme temperature events based on the NSDE thresholds, indicating that under SDE, these events occur approximately 2, 3, and 10 times more frequently, respectively.

Table 2
Change in Top 10, 5, and 1% of Warmest Surface Skin Temperature Due to SDE During March–August, for WE, NE Domain, Respectively

NSDE		10%	5%	1%
SDE	WE	20	17	11
	NE	23	18	10

Note. The threshold temperature for each percentile in NSDE is used to determine the new percentile in SDE, from the cumulative distribution functions shown in Figure 10.

3.4. Comparison of Model Climatology to Observations

In this subsection, we compare model surface air temperature and snow cover fraction (SCF) to MERRA2 reanalysis, which include assimilation of observational-based precipitation forcing of the land. Because this study is focused on model sensitivity to SDE, we only provide a brief discussion of model biases, and how they may affect our results. For a comprehensive assessment of MERRA2 land products compared to observations, and other reanalysis products, the readers are referred to Reichle et al. (2017).

Compared to MERRA2, the model SDE climatology has a similar spatial distribution, but shows excessive SCF (>10–20%) and a cold bias of 5 °C or more over the extratropical land and the Himalayas during MAM (Figure S3). The SCF and surface temperature biases are significantly

reduced during JJA (Figure S4), indicating that they are closely related, for example, higher SCF and colder surface temperature. In spite of these model biases, YKLK found a good agreement of the seasonal distribution of the 10% SCF line in the GEOS5 model compared to MODIS observations, indicating that the migration of the snowline is reasonably well simulated. As shown in our results, SDE warms the land by 2 °C or more compared to NSDE. Hence, including SDE moves the model surface air temperature in the right direction, but not enough to remove the bias. The reasons for the model biases are not clear, and likely related to model snow-hydrology parameterization, and cloud feedback processes (Reichle et al., 2017). Because of these biases, the sensitivity of the model hydroclimate to SDE is likely model dependent. As such, only the qualitative aspects of the present results should be emphasized.

4. Summary and Discussion

Based on GEOS5 climate model simulations, we have provided new insights into how snow-darkening effects (SDE) by deposition of light-absorbing aerosols may affect hydroclimate feedback and extreme hot weather over Eurasia during boreal spring and summer. Results show that the SDE surface solar forcing and accelerated snowmelt are most pronounced near the seasonal snowline. As the snowline migrates from south to north during boreal spring and summer, SDE-affected regions span the entire extratropical Eurasia.

Overall, SDE induces a model climate shift, with a warmer annual mean surface skin temperature (1–2.5 °C) and a substantial reduction in soil wetness (4–8%) over vast regions of the Eurasian continent. The effects of SDE on seasonal and regional hydroclimate are very pronounced. Over western Eurasia (10–100°E, 40–60°N), SDE invigorates the surface energy and water balance by increasing net absorption of surface SW radiation (14.8 Wm^{-2}), leading to substantially warmer land surface temperatures during the melting season and drying of the land during the warming season. Averaged over the domain, the energy gained by the land via SDE-induced SW absorption is approximately balanced by the energy lost through longwave radiation, latent heat, and sensible heat fluxes. The earlier snowmelt associated with the warmer temperatures spawns a brief period of increased soil wetness during the melting season. During the warming season (JJA), the land is dried by a reduction in snowmelt due to reduced snow cover and mass, much of which was lost through the earlier melt. During the same period, shortwave warming by SDE due to the loss of snow cover is diminished, but warming is nonetheless maintained by reduced cloudiness associated with increased atmospheric dryness, and the land continues to dry given the reduced snowmelt and increased evaporation loss. Similar SDE impacts are found over northern Eurasia (40–140°E, 60–75°N), except that the warming and drying of the land and atmosphere take place in later calendar months and over a shorter period because of its higher-latitude location.

Our results show that SDE-induced regional warming and prolonged drying over extratropical Eurasia is underpinned by a wet-first-dry-later (WFDL) mechanism (Figure 15). During the melting season, increased absorption of SW radiation by SDE adds energy to the land surface and increases snowmelt, leading to an initial increase in soil wetness along the seasonally northward migrating snowline in boreal spring and summer. Snow-albedo feedback enhances the surface warming, accelerating the snowmelt, and wetting of the soil on fast time scales (days to weeks). Because of conservation of water mass, the excess snow melted during the melting season results in less snow cover and amount in later months; hence, there is less water available from snowmelt during the beginning of the warming season, causing anomalous drying of the land at that point. As the snowline sweeps through Eurasia from south to north during the boreal spring and summer, it left behind large areas of reduced snow cover or exposed land surface, where land drying is sustained via land-atmosphere interaction through the warming season.

The SDE-induced atmosphere-land interaction are manifest in a reduction in atmospheric relative humidity and cloudiness and the establishment of seasonal mean conditions with higher tropospheric pressure and increased large-scale atmospheric subsidence, favorable for development of atmospheric blocking and heat waves during boreal summer. Stronger subsidence will increase adiabatic warming of the atmosphere, burn off more clouds, and expose the land surface to more shortwave radiation, thus providing a positive feedback to the warming and drying of the land-atmosphere system during boreal summer. WFDL also increases the probabilities of hot and dry weather extremes over western Europe and northern Eurasia, increasing the frequency of 10, 5, and 1% extreme hot days (as defined by NSDE thresholds) by approximately 2, 3, and 10 times, respectively.

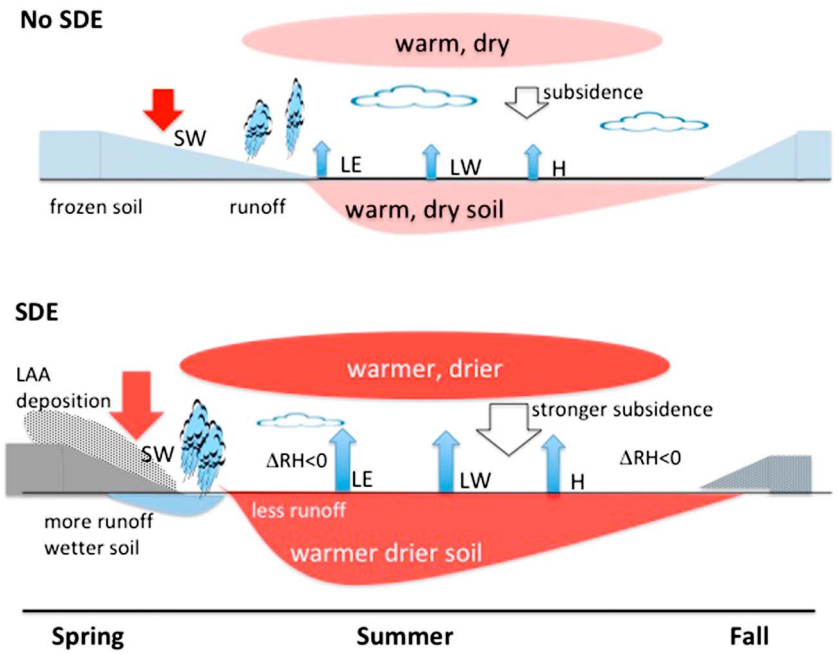

Figure 15. A schematic showing the wet-first-dry-later (WFDL) hydroclimate feedback mechanism due to SDE by light-absorbing aerosols (LAA) in accelerating melting of Eurasian snow cover during boreal spring, invigorating the surface energy exchanges, and facilitating the development of atmospheric conditions conducive to extreme hot dry weather during the following summer season. RH, SW, LW, *LE*, and *H* represent atmospheric relative humidity, net land surface solar radiation, longwave radiation, latent, and sensible fluxes, respectively. Timing and duration of the WFDL is a strong function of latitude, with melting and warming anomalies at higher latitudes occurring later in the season and over a shorter duration.

As a caveat, we note that because of the model biases, for example, excessive snow cover, and colder surface temperature, quantitative estimates of local and regional impacts are likely to be model dependent. Hence, the WFDL can only be viewed as a plausible mechanism for continental scale drying, with potential impacts on boreal summer heat waves—a working hypothesis that needs further tested through observational and model intercomparison studies.

Finally, our results are relevant in the context of previous observational studies on snow melting, soil moisture, and aerosols. Derksen and Brown (2012) found significant reduction spring of snow cover in Eurasia and North America in recent decades that maybe related to a warming and drier climate. Westerling et al. (2006) showed that earlier snow melting and increased spring and summer temperatures can be linked to increased wildfire frequency over the western United States. Jiang et al. (2016) found significant change in snow and cloud albedo due to open fire aerosols that may have impacts on climate change in Arctic regions. In view of the abundance of dust, BC, and OC aerosols derived from both natural and anthropogenic sources, SDE by deposition of light-absorbing aerosols could lead to conditions conducive to summertime wildfires, drought, and heat waves over northern hemisphere midlatitude continents, as well as affecting Arctic warming and drying (Serreze et al., 2003). These are topics worthy of further research.

Acknowledgments
This work was supported by the Modeling Analysis and Prediction (MAP) Program, Earth Science Division, NASA Headquarters. This work was partially funded by the Korea Meteorological Administration Research and Development Program under grant KMI2018-03410. M.K. Kim was supported by a sabbatical research grant of Kongju National University. Model output data and analysis data for this research are available at ftp://210.106.80.195/JGR_LAU_et_al_2018. Please contact J. Sang (j.sang0226@gmail.com) for questions regarding data accessibility.

References

Aoki, T., Kuchiki, K., Niwano, M., Kodama, Y., Hosaka, M., & Tanaka, T. (2011). Physically based snow albedo model for calculating broadband albedos and the solar heating profile in snowpack for general circulation models. *Journal of Geophysical Research: Atmospheres*, *116*(D11), 1–22. https://doi.org/10.1029/2010JD015507

Barnett, T. P., Dümenil, L., Schlese, U., Roekner, E., & Latif, M. (1989). The effect of Eurasian snow cover on regional and global climate variations. *Journal of the Atmospheric Sciences*, *46*(5), 661–686. https://doi.org/10.1175/1520-0469(1989)046<0661:TEOESC>2.0.CO;2

Barriopedro, D., Fischer, E. M., Luterbacher, J., Trigo, R. M., & Garcia-Herrera, R. (2011). The hot summer of 2010: Redrawing the temperature record map of Europe. *Science*, *332*(6026), 220–224. https://doi.org/10.1126/science.1201224

Beniston, M., & Coauthors (2007). Future extreme events in European climate: An exploration of regional climate model projections. *Climate Change*, *81*(S1), 71–95. https://doi.org/10.1007/s10584-006-9226-z

Black, E., Blackburn, M., Harrison, R. G., Hoskins, B. J., & Methven, J. (2004). Factors contributing to the 2003 summer European heatwave. *Weather*, *59*(8), 217–223. https://doi.org/10.1256/wea.74.04

Chin, M., Ginoux, P., Kinne, S., Torres, O., Holben, B. N., Duncan, B. N., et al. (2002). Tropospheric aerosol optical thickness from the GOCART model and comparisons with satellite and Sun photometer measurements. *Journal of the Atmospheric Sciences*, *59*(3), 461–483. https://doi.org/10.1175/1520-0469(2002)059<0461:TAOTFT>2.0.CO;2

Chin, M., Rood, R. B., Lin, S.-J., Müller, J.-F., & Thompson, A. M. (2000). Atmospheric sulfur cycle simulated in the global model GOCART: Model description and global properties. *Journal of Geophysical Research*, *105*(D20), 24,671–24,687. https://doi.org/10.1029/2000JD900384

Colarco, P., Da Silva, A., Chin, M., & Diehl, T. (2010). Online simulations of global aerosol distributions in the NASA GEOS-4 model and comparisons to satellite and ground-based aerosol optical depth. *Journal of Geophysical Research: Atmospheres*, *115*(D14), D14207. https://doi.org/10.1029/2009JD012820

Dang, C., Warren, S. G., Fu, Q., Doherty, S. J., Sturm, M., & Su, J. (2017). Measurements of light-absorbing particles in snow across the Arctic, North America, and China: Effects on surface albedo. *Journal of Geophysical Research: Atmospheres*, *122*(19), 10,149–10,168. https://doi.org/10.1002/2017JD027070

Derksen, C., & Brown, R. (2012). Spring snow cover extent reductions in the 2008–2012 period exceeding climate model projections. *Geophysical Research Letters*, *39*, L19504. https://doi.org/10.1029/2012GL053387

Ducharne, A., Koster, R. D., Suarez, M. J., Stieglitz, M., & Kumar, P. (2000). A catchment-based approach to modeling land surface processes in a general circulation model: 2. Parameter estimation and model demonstration. *Journal of Geophysical Research*, *105*, 823–824.

Dutra, E., Schär, C., Viterbo, P., & Miranda, P. M. A. (2011). Land-atmosphere coupling associated with snow cover. *Geophysical Research Letters*, *38*(15), L15707. https://doi.org/10.1029/2011GL048435

Fang, J., & Yang, X.-Q. (2016). Structure and dynamics of decadal anomalies in the wintertime midlatitude North Pacific Ocean-atmosphere system. *Climate Dynamics*, *47*(5-6), 1989–2007. https://doi.org/10.1007/s00382-015-2946-x

Fasullo, J. (2012). A mechanism for land-ocean contrasts in global monsoon trends in a warming climate. *Climate Dynamics*, *39*(5), 1137–1147. https://doi.org/10.1007/s00382-011-1270-3

Ferranti, L., & Viterbo, P. (2006). The European summer of 2003: Sensitivity to soil water initial conditions. *Journal of Climate*, *19*(15), 3659–3680. https://doi.org/10.1175/JCLI3810.1

Fischer, E. M., Seneviratne, S. I., Vidale, P. L., Lüthi, D., & Schär, C. (2007). Soil moisture-atmosphere interactions during the 2003 European summer heat wave. *Journal of Climate*, *20*(20), 5081–5099. https://doi.org/10.1175/JCLI4288.1

Flanner, M. G., Zender, C. S., Hess, P. G., Mahowald, N. M., Painter, T. H., Ramanathan, V., & Rasch, P. J. (2009). Springtime warming and reduced snow cover from carbonaceous particles. *Atmospheric Chemistry and Physics*, *9*(7), 2481–2497. https://doi.org/10.5194/acp-9-2481-2009

Flanner, M. G., Zender, C. S., Randerson, J. T., & Rasch, P. J. (2007). Present-day climate forcing and response from black carbon in snow. *Journal of Geophysical Research: Atmospheres*, *112*(D11), 2156–2202. https://doi.org/10.1029/2006JD008003

Gautam, R., Hsu, N. C., Lau, W. K.-M., & Yasunari, T. J. (2013). Satellite observations of desert dust-induced Himalayan snow darkening. *Geophysical Research Letters*, *40*, 988–993. https://doi.org/10.1002/grl.50226

Ginoux, P., Chin, M., Tegen, I., Prospero, J. M., Holben, B., Dubovik, O., & Lin, S.-J. (2001). Sources and distributions of dust aerosols simulated with the GOCART model. *Journal of Geophysical Research*, *106*(D17), 20,255–20,273. https://doi.org/10.1029/2000JD000053

Girardin, M. P., Ali, A., Carcaillet, C., Mudelsee, M., Drobyshev, I., Hély, C., & Bergeron, Y. (2009). Heterogeneous response of circumboreal wildfire risk to climate change since the early 1900s. *Global Change Biology*, *15*(11), 2751–2769. https://doi.org/10.1111/j.1365-2486.2009.01869.x

Groisman, P. Y., Karl, T. R., & Knight, R. W. (1994). Observed impact of snow cover on heat balance and the rise of continental spring temperatures. *Science*, *263*(5144), 198–200. https://doi.org/10.1126/science.263.5144.198

Hahn, D. G., & Shukla, J. (1976). An apparent relationship between Eurasian snow cover and Indian monsoon rainfall. *Journal of the Atmospheric Sciences*, *33*(12), 2461–2462. https://doi.org/10.1175/1520-0469(1976)033<2461:AARBES>2.0.CO;2

IPCC (2013). Climate Change 2013: The Physical Science Basis. Contribution of Working Group I to the Fifth Assessment Report of the Intergovernmental Panel on Climate Change. In T. F. Stocker et al. (Eds.) (1535 pp.). Cambridge, UK and New York: Cambridge University Press. https://doi.org/10.1017/CBO97811107415324

Jiang, Y., Lu, Z., Liu, X., Qian, Y., Zhang, K., Wang, Y., & Yang, X. Q. (2016). Impacts of global open-fire aerosols on direct radiative, cloud and surface-albedo effects simulated with CAM5. *Atmospheric Chemistry and Physics*, *16*(23), 14,805–14,824. https://doi.org/10.5194/acp-16-14805-2016

Jiang, Y., Yang, X.-Q., Liu, X., Yang, D., Sun, X., Wang, M., et al. (2017). Anthropogenic aerosol effects on east Asian winter monsoon: The role of black carbon-induced Tibetan Plateau warming. *Journal of Geophysical Research: Atmospheres*, *122*(11), 5883–5902. https://doi.org/10.1002/2016JD026237

Koster, R. D., Chang, Y., Wang, H., & Schubert, S. D. (2016). Impacts of local soil moisture anomalies on the atmospheric circulation and on remote surface meteorological fields during boreal summer: A comprehensive analysis over North America. *Journal of Climate*, *29*(20), 7345–7364. https://doi.org/10.1175/JCLI-D-16-0192.1

Koster, R. D., Suarez, M. J., Ducharne, A., Stieglitz, M., & Kumar, P. (2000). A catchment-based approach to modeling land surface processes in a general circulation model 1. Model structure. *Journal of Geophysical Research*, *105*(D20), 24,809–24,822. https://doi.org/10.1029/2000jd900327

Koster, R. D., Suarez, M. J., & Schubert, S. D. (2006). Distinct hydrological signatures in observed historical temperature fields. *Journal of Hydrometeorology*, *7*(5), 1061–1075. https://doi.org/10.1175/JHM530.1

Lau, K. M., & Bua, W. (1998). Mechanisms of monsoon-southern oscillation coupling: Insights from GCM experiments. *Climate Dynamics*, *14*(11), 759–779. https://doi.org/10.1007/s003820050253

Lau, K. M., & Kim, K. M. (2012). The 2010 Pakistan flood and Russian heat wave: Teleconnection of hydrometeorological extremes. *Journal of Hydrometeorology*, *13*(1), 392–403. https://doi.org/10.1175/JHM-D-11-016.1

Lau, K. M., & Kim, K. M. (2017). Competing influences of greenhouse warming and aerosols on Asian summer monsoon circulation and rainfall. *Asia-Pacific Journal of the Atmospheric Sciences*, *53*(2), 181–194. https://doi.org/10.1007/s13143-017-0033-4

Lau, N., & Nath, M. J. (2014). Model simulation and projection of European heat waves in present-day, and future climates. *Journal of Climate*, *27*, 3713–3730. https://doi.org/10.1175/JCLI-D-13-00284.1

Lee, W. S., Bhawar, R. L., Kim, M. K., & Sang, J. (2013). Study of aerosol effect on accelerated snow melting over the Tibetan Plateau during boreal spring. *Atmospheric Environment*, *75*, 113–122. https://doi.org/10.1016/j.atmosenv.2013.04.004

Lin, G., Penner, J. E., Flanner, M. G., Sillman, S., Xu, L., & Zhou, C. (2014). Radiative forcing of organic aerosol in the atmosphere and on snow: Effects of SOA and brown carbon. *Journal of Geophysical Research: Atmospheres*, *119*(12), 7453–7476. https://doi.org/10.1002/2013JD021186

Lorenz, R., Jaeger, E. B., & Seneviratne, S. I. (2010). Persistence of heat waves and its link to soil moisture memory. *Geophysical Research Letters*, *37*, L09703. https://doi.org/10.1029/2010GL042764

Luber, G., & McGeehin, M. (2008). Climate change and extreme heat events. *American Journal of Preventive Medicine*, *35*(5), 429–435. https://doi.org/10.1016/j.amepre.2008.08.021

Lynch-Stieglitz, M. (1994). The development and validation of a simple snow model for the GISS GCM. *Journal of Climate*, *7*(12), 1842–1855. https://doi.org/10.1175/1520-0442(1994)007<1842:TDAVOA>2.0.CO;2

Matsumura, S., & Yamazaki, K. (2012). Eurasian subarctic summer climate in response to anomalous snow cover. *Journal of Climate*, *25*(4), 1291–1303. https://doi.org/10.1175/2011JCL14116.1

Maurer, G. E., & Bowling, D. R. (2014). Seasonal snowpack characteristics influence soil temperature and water content at multiple scales in interior western U.S. mountain ecosystems, doi:https://doi.org/10.1002/2013WR014452.

Meehl, G., & Tebaldi, C. (2004). More intense, more frequent, and longer lasting heat waves in the 21st century. *Science*, *305*(5686), 994–997. https://doi.org/10.1126/science.1098704

Meehl, G. A. (1994). Influence of the land surface in the Asian summer monsoon: External conditions versus internal feedbacks. *Journal of Climate*, *7*(7), 1033–1049. https://doi.org/10.1175/1520-0442(1994)007<1033:IOTLSI>2.0.CO;2

Ménégoz, M., & Coauthors (2014). Snow cover sensitivity to black carbon deposition in the Himalayas: From atmospheric and ice core measurements to regional climate simulations. *Atmospheric Chemistry and Physics*, *14*(8), 4237–4249. https://doi.org/10.5194/acp-14-4237-2014

Nie, Y., Zhang, Y., Chen, G., Yang, & Yan, X.-Q. (2016). Delineating the barotropic and baroclinic mechanisms in the midlatitude eddy-driven jet response to lower-tropospheric thermal forcing. *Journal of the Atmospheric Sciences*, *73*(1), 429–448. https://doi.org/10.1175/JAS-D-15-0090.1

Painter, T. H., Deems, J. S., Belnap, J., Hamlet, A. F., Landry, C. C., & Udall, B. (2010). Response of Colorado River runoff to dust radiative forcing in snow. *Proceedings of the National Academy of Sciences*, *107*(40), 17,125–17,130. https://doi.org/10.1073/pnas.0913139107

Qian, Y., Flanner, M. G., Leung, L. R., & Wang, W. (2011). Sensitivity studies on the impacts of Tibetan Plateau snowpack pollution on the Asian hydrological cycle and monsoon climate. *Atmospheric Chemistry and Physics*, *11*(5), 1929–1948. https://doi.org/10.5194/acp-11-1929-2011

Qian, Y., Yasunari, T. J., Doherty, S. J., Flanner, M. G., Lau, W. K. M., Ming, J., et al. (2014). Light-absorbing particles in snow and ice: measurement and modeling of climatic and hydrological impact. *Advances in Atmospheric Sciences*, *32*(1), 64–91. https://doi.org/10.1007/s00376-014-0010-0

Randles, C. A., Colarco, P. R., & Da Silva, A. (2013). Direct and semi-direct aerosol effects in the NASA GEOS-5 AGCM: Aerosol-climate interactions due to prognostic versus prescribed aerosols. *Journal of Geophysical Research: Atmospheres*, *118*(1), 149–169. https://doi.org/10.1029/2012JD018388

Reichle, R., Draper, H. C., Liu, Q., Girotto, M., Mahanama, S., Koster, R., & De Lannoy, G. (2017). Assessment of MERRA-2 land surface hydrology estimates. *Journal of Climate*, *30*(8), 2937–2960. https://doi.org/10.1175/JCLI-D-16-0720.1

Reynolds, R. W., Rayner, N. A., Smith, T. M., Stokes, D. C., & Wang, W. (2002). An improved in situ and satellite SST analysis for climate. *Journal of Climate*, *15*(13), 1609–1625. https://doi.org/10.1175/1520-0442(2002)015<1609:AIISAS>2.0.CO;2

Rienecker, M. M., & Coauthors. (2008). The GEOS-5 Data Assimilation System—Documentation of versions 5.0.1 and 5.1.0, and 5.2.0. NASA Tech. Rep. Series on Global Modeling and Data Assimilation, NASA/TM-2008-104606, Vol. 27, 92 pp.

Schubert, S. D., Wang, H., Koster, R. D., Suarez, M. J., & Groisman, P. (2014). Northern Eurasian Heat waves and droughts. *Journal of Climate*, *27*(9), 3169–3207. https://doi.org/10.1175/JCLI-D-13-00360.1

Seneviratne, S. I., Lüthi, D., Litschi, M., & Schär, C. (2006). Land-atmosphere coupling and climate change in Europe. *Nature*, *443*(7108), 205–209. https://doi.org/10.1038/nature05095

Serreze, M. C., Bromwich, D. H., Clark, M. P. A., Ertringer, J., Zhang, T., & Lammers, R. (2003). Large-scale hydro-climatology of the terrestrial Arctic drainage system. *Journal of Geophysical Research*, *108*(D2), 8160. https://doi.org/10.1029/2001JD000919

Tomczyk, A. M., & Bednorz, E. (2016). Heat waves in Central Europe and their circulation conditions. *International Journal of Climatology*, *36*(2), 770–782. https://doi.org/10.1002/joc.4381

Trenberth, K. E., & Fasullo, J. T. (2012). Climate extremes and climate change: The Russian heat wave and other climate extremes of 2010. *Journal of Geophysical Research: Atmospheres*, *117*(D17), 1–12. https://doi.org/10.1029/2012JD018020

Warren, S. G., & Wiscombe, J. W. (1980). A model for the spectral albedo of snow. 2: Snow containing atmospheric aerosols. *Journal of the Atmospheric Sciences*, *37*(12), 2734–2745. https://doi.org/10.1175/1520-0469(1980)037<2734:AMFTSA>2.0.CO;2

Westerling, A. L., Hidalgo, H. G., Cayan, D. R., & Swetnam, T. W. (2006). Warming and earlier spring increase western U.S. forest wildfire activity. *Science*, *313*(5789), 940–943. https://doi.org/10.1126/science.1128834

Xu, J., Grumbine, R. E., Shrestha, A., Eriksson, M., Yang, X., Wang, Y., & Wilkes, A. (2009). The melting Himalayas: Cascading effects of climate change on water, biodiversity, and livelihoods. *Conservation Biology*, *23*(3), 520–530. https://doi.org/10.1111/j.1523-1739.2009.01237.x

Xue, Y., Vasic, R., Janjic, Z., Liu, Y. M., & Chu, P. C. (2012). The impact of spring subsurface soil temperature anomaly in the Western U.S. on North American summer precipitation—A case study using regional climate model downscaling. *Journal of Geophysical Research*, *117*, D11103. https://doi.org/10.1029/2012JD017692

Yasunari, T., Kitoh, A., & Tokioka, T. (1991). Local and remote responses to excessive snow mass over Eurasia appearing in the northern spring and summer climate. *Journal of the Meteorological Society of Japan*, *69*(4), 473–487. https://doi.org/10.2151/jmsj1965.69.4_473

Yasunari, T. J., & Coauthors (2010). Estimated impact of black carbon deposition during pre-monsoon season from Nepal climate observatory—Pyramid data and snow albedo changes over Himalayan glaciers. *Atmospheric Chemistry and Physics*, *10*(14), 6603–6615. https://doi.org/10.5194/acp-10-6603-2010

Yasunari, T. J., & Coauthors (2013). Estimated range of black carbon dry deposition and the related snow albedo reduction over Himalayan glaciers during dry pre-monsoon periods. *Atmospheric Environment*, *78*, 259–267. https://doi.org/10.1016/j.atmosenv.2012.03.031

Yasunari, T. J., & Coauthors (2014). The GOddard SnoW impurity module (GOSWIM) for the NASA GEOS-5 earth system model: Preliminary comparisons with observations in Sapporo, Japan. *Solaiat*, *10*(0), 50–56. https://doi.org/10.2151/sola.2014-011

Yasunari, T. J., Koster, R. D., Lau, W. K. M., Aoki, T., Sud, Y. C., Yamazaki, T., et al. (2011). Influence of dust and black carbon on the snow albedo in the NASA Goddard earth observing system version 5 land surface model. *Journal of Geophysical Research: Atmospheres*, *116*(D2), 1–15. https://doi.org/10.1029/2010JD014861

Yasunari, T. J., Koster, R. D., Lau, W. K. M., & Kim, K.-M. (2015). Impact of snow darkening via dust, black carbon, and organic carbon on boreal spring climate in the earth system. *Journal of Geophysical Research: Atmospheres*, *120*(11), 5485–5503. https://doi.org/10.1002/2014JD022977

Yeh, T.-C., Wetherald, R. T., & Manabe, S. (1983). A model study of the short-term climatic and hydrologic effects of sudden snow-cover removal. *Monthly Weather Review*, *111*(5), 1013–1024. https://doi.org/10.1175/1520-0493(1983)111<1013:AMSOTS>2.0.CO;2